Journal of Physics and Chemistry of Solids 211 (2026) 113411

Contents lists available at ScienceDirect

Journal of Physics and Chemistry of Solids

journal homepage: www.elsevier.com/locate/jpcs

# Rate –limiting steps of the oxygen reduction reaction in $REBa_2Cu_3O_{6+\delta}$ (RE = La, Nd, Sm, Gd and Y) layered perovskites as IT-SOFC cathodes

J. Grassi [a,b], A. Montenegro-Hernandez [c], A.C. Serquis [c], J.F. Basbus [d,*], L. Suescun [a]

[a] Cryssmat-Lab/DETEMA, Facultad de Química, Universidad de La República, Av. Gral. Flores 2124, Montevideo, 11800, Uruguay
[b] Centro Tecnológico ENERGYLAB, Edificio CITEXVI, Rua Fonte Das Abelleiras, s/n, Vigo, 363310, Pontevedra, Spain
[c] Departamento Caracterización de Materiales (DCM), Centro Atómico Bariloche (CAB), Comisión Nacional de Energía Atómica (CNEA), Av. Bustillo 9500, San Carlos de Bariloche, Río Negro, 8400, Argentina
[d] Aragon Nanoscience and Materials Institute (INMA), Higher Council for Scientific Research (CSIC), University of Zaragoza (UniZar) and Condensed Matter Physics Department, C/Pedro Cerbuna 12, 50009, Zaragoza, Spain

ARTICLE INFO

*Keywords:*
Perovskite
IT SOFC cathode
Ionic radii
Oxygen reduction reaction
Co-free

ABSTRACT

The classical high-temperature superconductor $YBa_2Cu_3O_{6+\delta}$ (YBCO) with an oxygen-vacant triple perovskite structure has been proposed as a potential cathode for Intermediate Temperature Solid Oxide Fuel Cells (IT-SOFCs), and $REBa_2Cu_3O_{6+\delta}$ (RE = La, Nd, Sm, Gd and Y) triple perovskites synthesized by a self-combustion method were evaluated. The total substitution of Y by lanthanide ions ($RE^{3+}$) proved to modify relevant bulk and surface properties, thus changing performance under operating conditions, i.e., the incorporation–diffusion mechanism by oxygen vacancies and oxide anion transport. Electrochemical Impedance Spectroscopy (EIS) under different oxygen partial pressure ($pO_2$) and temperature (T) conditions allowed elucidating a co-limited oxygen incorporation/diffusion mechanism as Oxygen-Reduction Reaction (ORR) limiting steps. Ionic radii ($r_i$) variation from $Y^{3+}$ to $La^{3+}$ impacts the kinetics of the two steps, thereby modifying the overall cathode performance. The results provide evidence of the complex relationship between crystallography, point defect concentration, chemical composition and electrochemical properties in REBCO cathodes. Data suggest that the Cu–O bond distance in cuprates may be critical for shifting the rate-limiting step and improving ORR activity. Overall, this research advances the comprehension of ORR kinetics in cobalt-free materials with layered diffusion.

## 1. Introduction

Intermediate temperature solid oxide fuel cells (IT-SOFCs) have shown a remarkable technological evolution in recent years [1–3]. Microstructural aspects, chemical and mechanical long-term stability and electrochemical performance are essential factors determining the suitability of materials as electrodes for these devices. Cathode materials present particular electrochemical significance in IT-SOFCs, where the oxygen reduction reaction (ORR) contributes significantly to the overpotential losses.

Among ceramic compounds with the highest electrochemical performance reported in the literature are layered oxygen-deficient perovskites (LODP), which contain cobalt in their crystal structure [4]. The presence of aliovalent cobalt ($Co^{2+}/Co^{3+}$ or $Co^{3+}/Co^{4+}$ pairs) within the structure gives cobaltites high electrical conductivity, and the large number of mobile oxygen vacancies observed confers significant ionic conductivity [4–6], enhancing their high electrocatalytic activity concerning the ORR. Nevertheless, a drawback of using Co perovskites lies in a pronounced mismatch between the Thermal Expansion Coefficients (TEC) values and commonly used electrolytes [4,7–9]. Another important aspect is the scarcity of Co and the indiscriminate exploitation of this metal in regions characterized by extreme poverty and deplorable health conditions.

Investigation of Co-free materials, such as cuprates or nickelates, has yielded comparable or superior results in some cases. Promising results have also been obtained by substituting cobalt with iron [10,11]. Nickelates adopting the form of $Ln_2NiO_{4+\delta}$ [12] and cuprates with a $La_{1.5}Ba_{1.5}Cu_3O_{7\pm\delta}$ [9], $LaNi_{1-x}Cu_xO_{3-\delta}$ [13], and $La_4BaCu_5O_{13\pm\delta}$ [14] structures have shown not only elevated electrochemical performance but also lower TEC values similar to those of $Ce_{0.8}Gd_{0.2}O_{1.95}$ (GDC),

* Corresponding author.
*E-mail address:* juan.basbus@csic.es (J.F. Basbus).

https://doi.org/10.1016/j.jpcs.2025.113411
Received 14 October 2025; Received in revised form 5 November 2025; Accepted 26 November 2025
Available online 2 December 2025

$LaSr_{0.2}Ga_{0.8}Mg_{0.2}O_{3-\delta}$ (LSGM), and $Ce_{0.8}SmO_{1.95}$ (SDC) electrolytes [15]. Otherwise, the promising $BaSr_{0.5}FeCu_{0.2}O_{3-\delta}$ cathode presented a reasonable total conductivity value but a TEC mismatch with common IT-SOFC electrolytes [16].

The traditional $La_2CuO_{4+\delta}$ cuprate has been referred to in the literature as the T phase, wherein, analogous to other Ruddlesden-Popper (RP) type structures, Cu (B-site) occupies an axially distorted octahedral site [17]. The structure can be visualized as an intercalated perovskite and rock salt layers of $La_2O_2$ slabs. Tetrahedral holes between these layers facilitate oxygen over stoichiometry (δ), which promotes ionic diffusion within the structure. Consequently, layered cuprates occasionally perform better than other perovskite-type oxides [18].

Studies in layered perovskites based on $LnBa_{0.5}Sr_{0.5}Cu_2O_{5+\delta}$ (Ln = Pr and Nd) [19], where materials with La substituted by Pr and Nd were evaluated, exhibited significant maximum power density values. Li et al. reported that introducing Ba into the La site enhances the electrochemical performance of the cathode, yielding values approaching 500 mW•cm-2 at 800 °C [9]. Other authors investigated differences between undoped and $Ba^{2+}$-doped RP phases of $La_2CuO_{4+\delta}$, revealing shifts in rate-limiting steps (RLS) of the ORR product of this modification [20]. An important conclusion of the above work is the elucidation that incorporating Ba into the crystal structure reduces the energy required for oxygen vacancy formation.

Intending to use cobalt-free materials, we have investigated Cu-containing perovskites with mixed ionic-electronic conductivity (MIEC). $YBa_2Cu_3O_{6+\delta}$ (YBCO) is a well-known triple perovskite displaying high temperature superconductivity (HTc) below 90K when $\delta \approx 1$ [21]. It presents a layered structure with remarkably anisotropic diffusion properties characterized by a high mobile oxygen vacancy density above 400 °C and broad oxygen nonstoichiometry ($0 < \delta < 1$) combined with intrinsic oxygen-vacant sites. In previous work, we have characterized YBCO [22] and REBCO (RE = La, Nd, Sm, Gd and) materials as cathodes for IT-SOFCs [23] and found that the substitution of Y by the other RE degrades the electrochemical performance of the test cells, reducing power density. Cordaro et al. investigated in 2019 the $PrBa_2Cu_3O_{7-\delta}$ perovskite as cathode material, concluding that samples produced with different cooling rates showed that different O/T ratios influence the oxygen content (6+δ), the electrical conductivity and the polarization resistances [24].

In this previous work, the parameters obtained for the equivalent circuit elements of the calculated equivalent circuit model (ECM) for REBCO samples varying temperature under constant pressure ($pO_2 \sim 0.2$ atm) indicated that surface oxygen kinetic incorporation was favoured for those containing larger ionic $RE^{3+}$. In contrast, the ionic diffusion component in the structure exhibits an opposite behavior. This behavior was not expected based only on structural considerations, pushing us to delve deeper into the mechanisms of the oxygen-reduction reaction (ORR). This work presents a detailed study of rare-earth (RE) element substitution's effect on REBCO (RE = La, Nd, Sm, Gd and Y) compounds performed by temperature and oxygen partial pressure dependent electrochemical spectroscopy.

## 2. Experimental

### 2.1. Materials preparation

REBCO (RE = La, Nd, Sm, Gd and Y) triple-layered perovskites were synthesized according to the procedure described in Ref. [23]. Stoichiometric amounts of nitrates of the rare earth RE $(NO_3)_3{\cdot}6H_2O$ (Sigma-Aldrich >99.0 %), $Ba(NO_3)_2$, and $Cu(NO_3)_2$ (Sigma-Aldrich >99.0 %), were dissolved in distilled water at room temperature (RT). EDTA (Sigma Aldrich >99.4 %) 1:1,1 M ratio, and ammonium nitrate $NH_4NO_3$ were added as a chelating agent and combustion trigger, respectively. The solution was heated on a hot plate at 120 °C under magnetic stirring until a blue gel formed. The gel was dried and burned directly in the beaker at 300 °C until a black foam-like ash was obtained. The final thermal treatment to obtain the electrode material was performed at 850 °C in air using a 5 °$Cmin^{-1}$ ramp. The obtained materials resulted in homogeneous fine-grain sub-micrometric powders displaying the characteristic metallic-black colour for all the samples.

### 2.2. Structural characterization

The prepared samples were structurally characterized by X-ray diffraction (XRD) using a Rigaku ULTIMA IV diffractometer, with Cu-$K_\alpha$ radiation, working in Bragg–Brentano mode, in the angular range (2θ) of 5.0–100.00°, and 2θ steps of 0.02°. Patterns were collected in air and at RT and then fitted by Rietveld Method using GSAS II software [25] to confirm single-phase samples and cell parameters.

### 2.3. Symmetrical cell preparation

Commercial microstructured GDC electrolyte provided by Fiaxell SOFC Technologies was pressed into 13 mm pellets and sintered at 1400 °C for 12 h to prepare symmetric cells REBCO/GDC/REBCO for electrochemical characterization. Ink composition and electrode deposition are described in Ref. [23]. Two layers of the cathode slurry (on each side) were screen-printed on the electrolyte pellet and sintered at 900 °C for 4 h. The microstructure, adhesion of the electrode, particle size distribution, thickness and layer uniformity of the half-cells were characterized by Scanning Electron Microscopy (SEM) using a field emission gun (FEG) Nova NanoSEM 230. The particle size distribution was estimated using ImageJ software [26].

### 2.4. Electrochemical measurements and performance

The electrochemical performance of the different cathode composites was tested by Electrochemical Impedance Spectroscopy (EIS). The spectra were collected in ambient pressure conditions using a frequency response analyzer (FRA) coupled with a potentiostat/galvanostat PGSTAT30 between $10^{-2}$ and $1 \times 10^6$ Hz with 100 mV amplitude in OCV conditions. Data were evaluated by varying the temperature (T) and oxygen partial pressure ($pO_2$). Spectra were collected in a heating mode, from 600 to 800 °C. At each T, spectra were also acquired from high to low $pO_2$ values (i.e., from oxidizing to reducing conditions), from 1 to 0.0019 atm. The $pO_2$ values were controlled using an electrochemical device with an $O_2$/Ar gas mixture system coupled to a Zr pump sensor [27]. Samples were kept for 2 h at each T to ensure thermal equilibrium. In order to calculate the polarization resistance (Rp), impedance spectra were fitted using ZView4.0 Scribner Associates Inc. Software.

## 3. Results and discussion

### 3.1. Structural characterization

Fig. 1a and b shows the profile fitting of the XRD patterns for the synthesized $LaBa_2Cu_3O_{6+\delta}$ (LBCO) and $NdBa_2Cu_3O_{6+\delta}$ (NBCO) phases, respectively. Figs. S1 and S2 in the supplementary information (SI) show the profile fitting of Y, Gd and Sm cations. Fig. 1c illustrates the evolution of the (001) reflections for the different RE substitutions, showing the characteristic shift to small angles of the peak position due to the increase of unit cells in the c direction as the $RE^{3+}$ ionic radii ($r_i$) increase. Table 1 shows the nomenclature used for the REBCO perovskites, and Fig. S2 in the SI illustrates the orthorhombic YBCO phase with the atom labelling scheme. Rietveld refinement results and the corresponding diffraction patterns confirm that all samples prepared present a single-phase composition.

Fig. 2a) and b) show a structural representation of several unit cells of the triple layer $[Ba_2Cu_3O_{6+\delta}]^{3-}$ in the orthorhombic *Pmmm* oxygen-vacancy ordered $REBa_2Cu_3O_7$ (δ = 1) and the tetragonal P4/mmm oxygen-depleted $REBa_2Cu_3O_6$ (δ = 0) variants. In the REBCO structures

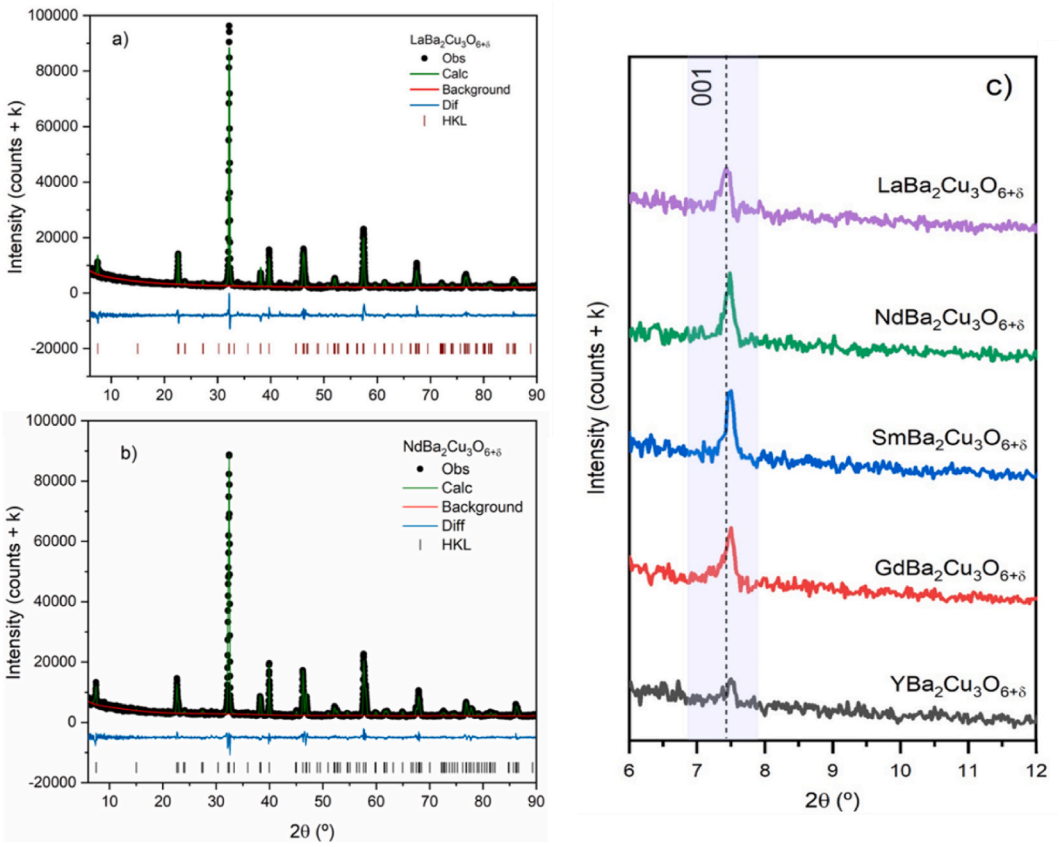


**Fig. 1.** Profile fitting by the Rietveld Method of a) LBCO and b) NBCO. c) Comparison among (001) Bragg peaks of as-prepared REBCO perovskites.

**Table 1**
Structural parameters obtained from Rietveld analysis for REBCO samples obtained at RT. The lattice parameters (a, b and c) and unit cell volume (V) are indicated.

| RE | Short Name | SG | $r^{3+}$(Å) | Cell parameters | | | |
|---|---|---|---|---|---|---|---|
| | | | | a (Å) | b (Å) | c (Å) | V (Å$^3$) |
| La | LBCO | *P4/mmm* | 1.360 | 3.927 (3) | 3.927 (3) | 11.798 (6) | 181.986 (4) |
| Nd | NBCO | *P4/mmm* | 1.246 | 3.918 (3) | 3.918 (3) | 11.634 (5) | 178.663 (4) |
| Sm | SBCO | *Pmmm* | 1.219 | 3.874 (2) | 3.904 (3) | 11.711 (6) | 177.164 (5) |
| Gd | GBCO | *Pmmm* | 1.193 | 3.842 (3) | 3.905 (3) | 11.711 (7) | 175.710 (4) |
| Y | YBCO | *Pmmm* | 1.159 | 3.831 (2) | 3.887 (3) | 11.682 (6) | 173.973 (5) |

and according to their oxygen stoichiometry (6+δ), Cu ions exhibit three electronic configurations: $d^8$, $d^9$, and $d^{10}$, occupying square-planar, pyramidal or linear chain environments respectively within a unit cell. When the system exhibits orthorhombic symmetry, the $Cu^{III}O$ squares form lines along the crystallographic b axis leading to an ordered oxygen vacancy system of rows along the a-axis (crystallographic sites 0,½,0 are vacant in the structure) (Fig. 2c). On the other hand, in the tetragonal structure, the planes described above are absent, and instead, linear $Cu^{I}$ centers connecting pyramids are present, where both crystallographic sites ½,0,0 and 0,½,0 are vacant (Fig. 2d).

In addition, oxide anion diffusion occurs between two vacancies located in the $CuO_8$ planes, specifically through the O–Cu–O path. Literature reports that the distance between these two crystallographic sites ($d_{O1\text{-}O1}$), the free volume ($V_f$) inside the perovskite structure and the B-site metal oxygen bond (B–O band) energy are highly relevant for evaluating the activation energy ($E_a$) involved in the oxide anion transport (see Fig. 2d) [28–30].

Table 1 lists the structural parameters of REBCO samples. For intermediate oxygen contents $0 < \delta < 1$ as the one found in our compounds (d ~ 0.5) [23], data show that samples containing smaller $RE^{3+}$ ($Gd^{3+}$ and $Y^{3+}$) crystallize in the orthorhombic *Pmmm* structure, whereas those with larger cations adopt a tetragonal *P4/mmm*, at room temperature. As previous work noted, the orthorhombic structure undergoes a second-order phase transition to the tetragonal structure between 350 and 450 °C in air, depending on $RE^{3+}$ [24,31]. The oxygen vacancy-ordered orthorhombic system gives place to an oxygen-vacancy-disordered tetragonal phase, where the O1 oxygen site in (0,1/2,0) position in the basal plane of the orthorhombic cell is disordered over (1/2,0,0) and (0,1/2,0) sites in the tetragonal one.

The results obtained for the prepared samples seem to be inconsistent with some of the data presented in the literature [30–32] when these materials were studied as HTc superconductors. Authors indicated that all $REBa_2Cu_3O_{6+\delta}$ structures crystallize in the *Pmmm* structure when synthesized through solid-state reaction, sol-gel methods and other soft chemical synthesis routes such as combustion using citrate. A possible explanation that justifies the observed difference lies in the microstructure of powders and particle size distribution when ceramics are prepared through the synthetic route chosen in this work. In addition, for high-temperature superconductivity to be observed, δ ~1 is required, while our compounds show lower oxygen nonstoichiometry.

This observation underlines the critical role of processing conditions in tailoring the crystallographic structure and, consequently, material

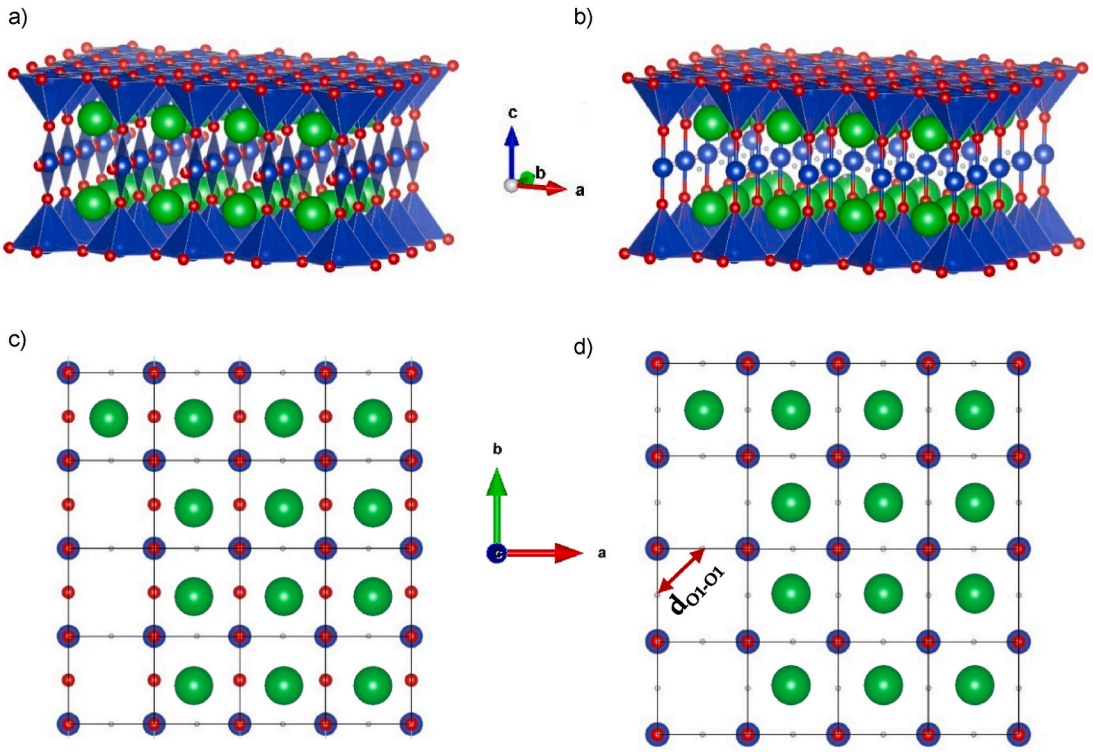


**Fig. 2.** Comparison between crystal structures of a) *Pmmm* orthorhombic ($REBCO_7$) and b) *P4/mmm* tetragonal ($REBCO_6$) forms of REBCO phases. Note the change from square coordination of $Cu^{III}O_4$ units in the orthorhombic structure and linear $Cu^{I}O_2$ in the tetragonal one. In the same way, the $CuO_8$ planes are shown for c) orthorhombic and d) tetragonal perovskite. Green, blue and red spheres correspond to Ba, Cu, and O atoms, respectively. (For interpretation of the references to colour in this figure legend, the reader is referred to the Web version of this article.)

properties. An important feature to remark regarding the sustained perovskite structure studied is that all REBCO samples, regardless of the $RE^{3+}$, preserve the tetragonal symmetry at SOFC operational conditions (500–800 °C) as reported in Ref. [23].

### 3.2. Microstructural characterization

Fig. 3 presents SEM images of the cross and normal sections of porous GBCO cathode deposited on the GDC as symmetrical cells. Cross-sectional images evidenced a coherent electrode/electrolyte interface, correct adhesion, porosity and uniformity of the deposited layers. Particle size distributions were estimated by the normal sections, and histograms revealed particle sizes predominantly ranging between 150 and 200 nm. All cathodes exhibit a similar particle size average and morphology, with no significant differences in the measured sizes based on RE ionic radii. No significant modifications in the particle size of the cathode material or contact between the electrode layer and the electrolyte-sintered pellet were observed in the configuration of the symmetrical button cells for all compositions. Fig. S3 in SI offer a comparative analysis of the morphology and particle size distribution for REBCO samples sintered at 900 °C in air for 4 h.

### 3.3. Electrochemical characterization

The correlation between the cathodic polarization resistance ($R_c$) and $pO_2$ on the electrode surface was investigated to allow a more detailed understanding of this effect. Generally, the relationship between these variables can be expressed as [31–35]:

$$R_c \propto pO_2^{-n} \quad (1)$$

where n represents a parameter of the RLS-ORR. The n value indicates a different elementary steps reaction order related to the transport mechanism: n = 1 is associated with molecular oxygen diffusion processes and adsorption on the electrode surface, n = 1/2 is associated with surface dissociation processes leading to the formation of 2 adsorbed neutral or charged O atoms, and $0 < n < 1/2$ values are linked to charge transfer reactions of adsorbed oxygen atoms followed by ionic incorporation at the interface between the electrode and the electrolyte. Literature also reports a more specific range of values $1/4 < n < 1/2$ (varying between 1/8 and 3/8) related to dissociation and charge transfer process at the electrode, known as dissociative adsorption on the electrode surface [36–38].

Fig. 4 compares the evolution of impedance spectra at different $pO_2$ for LBCO, NBCO, SBCO and GBCO samples at 600 °C (for 700 and 800 °C see Fig. S3 SI). It can be observed that $R_c$ increases with the decrease in $pO_2$, which is expected due to the limitation of oxygen reactive species near the electrode's surface. From Fig. 4, it can also be seen that irrespective of the specific $RE^{3+}$, the spectra consistently present a single, well-defined arc at higher $pO_2$ values. However, a decrease in $pO_2$ invariably leads to the emergence of a second, larger resistive contribution at lower frequencies. This phenomenon is systematically observed across all samples and at all investigated operation temperatures. Furthermore, Nyquist plots appear to distort noticeably with increasing temperature. This deformation suggests a variation in the capacitive component, related to the electrode's microstructure modification. This behaviour is probably attributed to the repeated oxidation-reduction cycling experienced by the electrode due to the variations in oxygen partial pressure. This microstructural alteration could affect relevant parameters, including active site availability, triple phase boundary length, or internal transport pathways, thereby influencing the overall electrochemical performance.

To get more insight into the ORR and to identify the RLS, EIS data were fitted using an equivalent circuit model (ECM) to identify individual contributions. Table 2 provides an illustrative overview of the equivalent circuit elements employed to fit the acquired spectra for the LBCO sample at 600, 700, and 800 °C (for the other samples, see Table 1

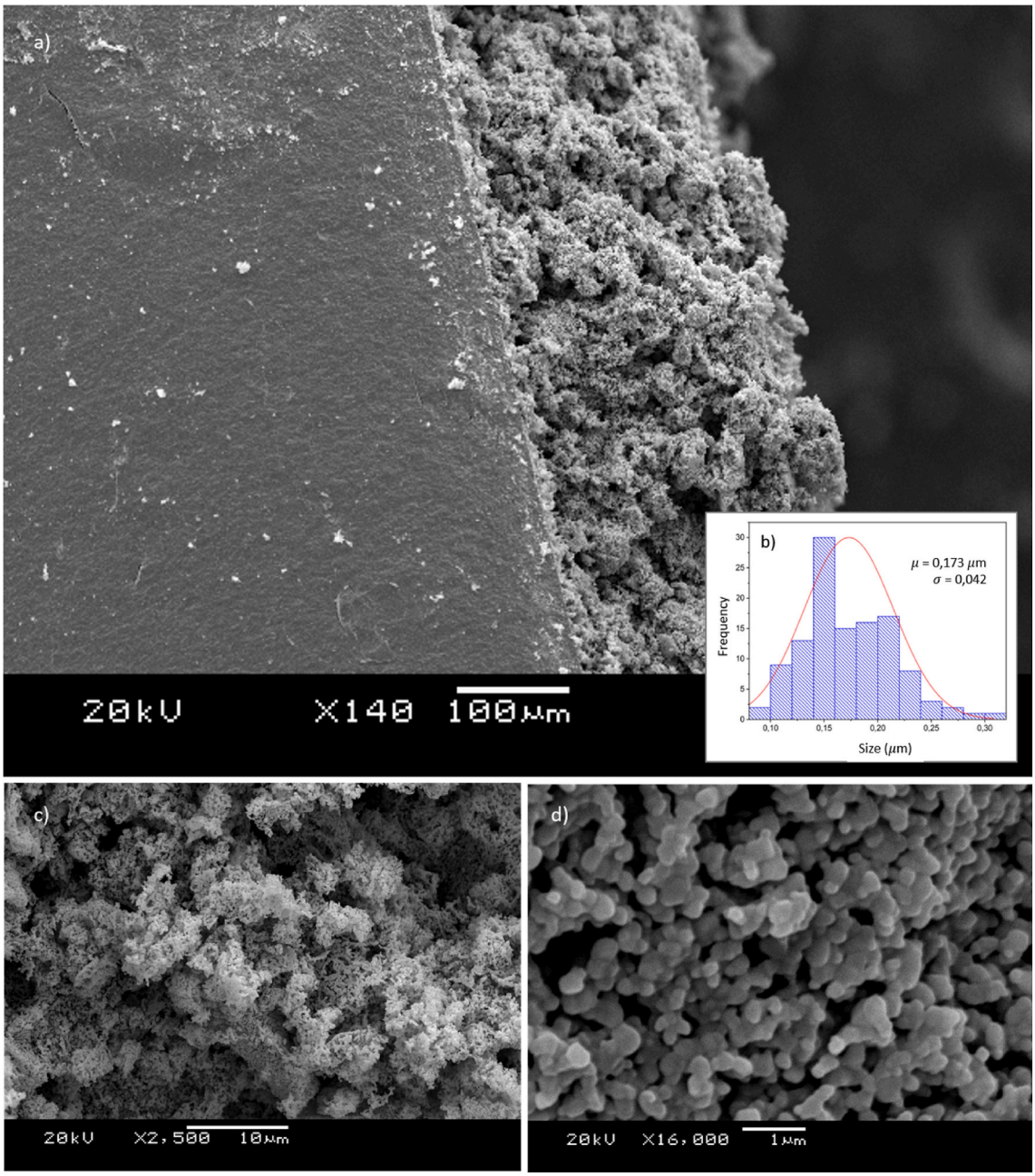


**Fig. 3.** SEM images of a) cross section and c) and d) normal sections of GBCO/GDC half-cell. b) Measured particle distribution.

SI). In all cases, an inductive element (L) was included to represent the circuit wiring (potentiostat, frequency analyzer and PC) in series with an ohmic resistance ($R_{el}$), which corresponds mainly to the electrolyte contribution. This ohmic component was subtracted from the spectra to simplify the comparison. The best fit was obtained using a Gerischer-type (G) element and a combination of one resistance in parallel with one constant-phase element (R//CPE) for the medium (MF) and low-frequency (LF) contributions (fits results can be consulted in SI Table S3).

The $R_{c-MF}$ component, derived from the $R_{c-MF}$//$CPE_{MF}$ pair, exhibits a monotonic evolution across all samples with decreasing oxygen partial pressure, regardless of temperature. As depicted in Fig. 5a and b, the **n** parameter varies between 0.35 and 0.50 at both 600 °C and 700 °C, with similar behavior observed for all samples, even at 800 °C. These variations, coupled with the obtained capacitance values ranging from 1 to $10^{-2}$ $Fcm^{-2}$, suggest that the rate-limiting steps in this range are the dissociative adsorption and mainly, charge transfer reaction steps [39, 40]. At 600 °C, medium-frequency polarization resistance values exhibit no clear correlation with the ionic radii of the $RE^{3+}$ species. Notably, $Sm^{3+}$ demonstrates the highest polarization resistance across the entire $pO_2$ range investigated. Furthermore, at 700 °C, a distinct relationship emerges among the cations in the series. Both $Y^{3+}$ and $Gd^{3+}$ exhibit the lowest charge transfer resistance. $Sm^{3+}$ appears to represent a transitional point concerning ionic radii. Data suggest that the sustained variation in the ionic radius of the cations does not significantly promote or improve charge transfer processes, at the electronic level, between the gas phase and the electrode surface. The observed behaviour for the REBCO samples is somewhat expected, as the electron transfer reactions take place at crystallographic sites occupied by Cu1 (see Fig. S1). Meanwhile, the cell dimensions, directly related to changes in the $RE^{3+}$ cation, apparently do not influence the reaction rate of oxidation/reduction of the $Cu^{2+/3+}$ ions.

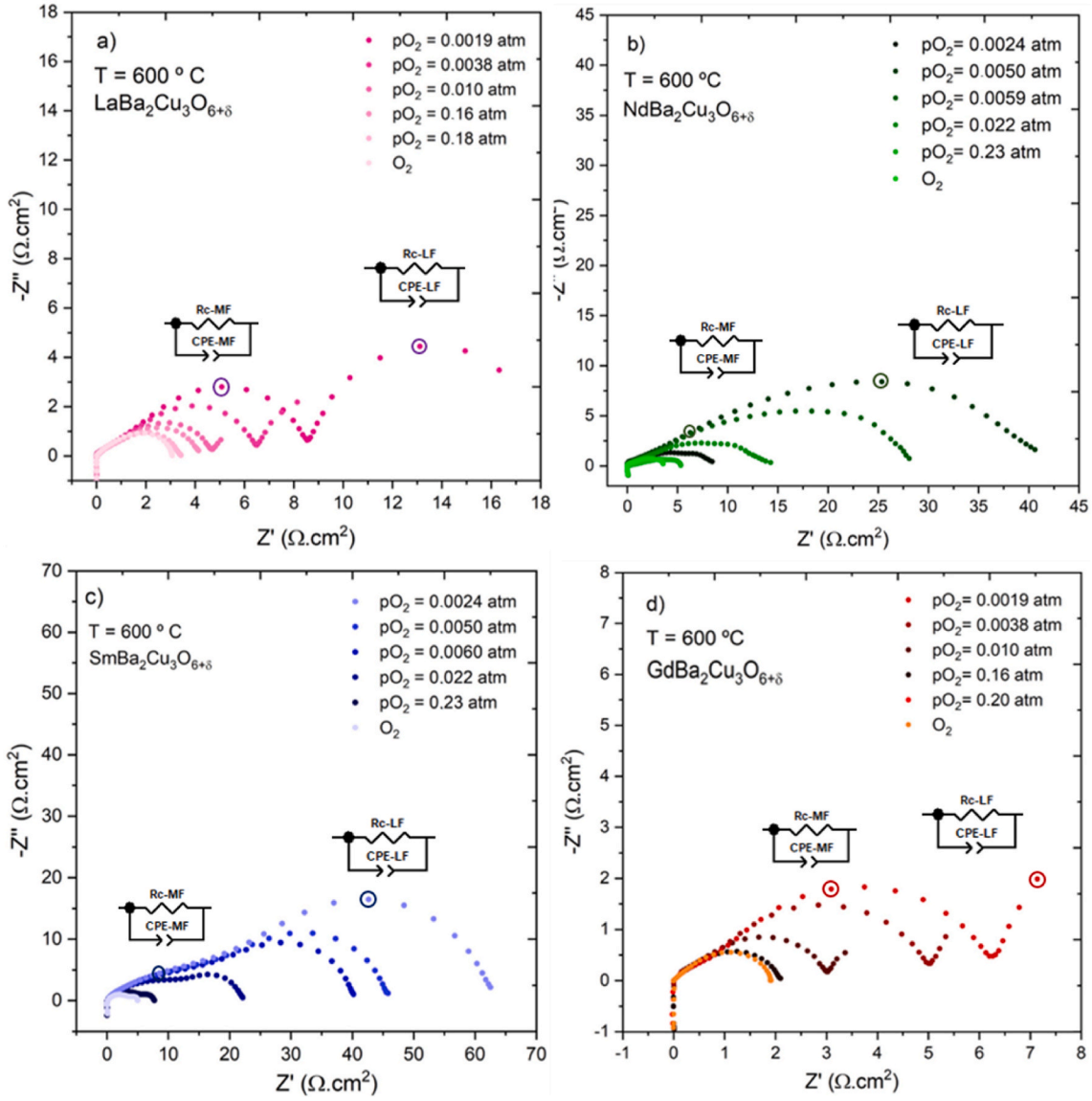


**Fig. 4.** Evolution of the Nyquist plot against $pO_2$ collected from REBCO-GDC symmetric cell configuration at 600 °C and different $pO_2$ values where: a) La, b) Nd, c) Sm and d) Gd.

**Table 2**
Equivalent circuit models as a function of T and $pO_2$ for LBCO cathode. L, R, G and CPE correspond to inductance, resistance, Gerischer element, and Constant Phase Element, respectively.

| LBCO | | | | | | |
|---|---|---|---|---|---|---|
| T (°C) | -log ($pO_2$) (atm) | | | | | |
| | 0 | 0.70 | 2 | 2.28 | 2.40 | 2.72 |
| **600** | | | | | | |
| **700** | 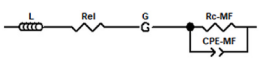 | | | 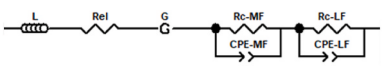 | | |
| **800** | | | | | | |



Fig. 5c and d illustrate the $R_{c-LF}$ evolution for 600 and 700 °C for all REBCO samples. The emergence of a new impedance arc at low frequencies ($R_{c-LF}$) and reduced $pO_2$ values can be attributed to the depletion of electrochemically active species concentration resulting from oxygen partial pressure decrease. The appearance of this third impedance arc under similar oxygen partial pressures has been widely reported in the literature [41–43]. This low-frequency component (approximately 0.1–1 Hz) could be associated with gaseous species ($O_2$) diffusion through the electrode's pores.

The low-frequency contribution at 600 °C exhibits a clear dependence where $0.9 < n < 1$ (see Fig. 5c), aligning with processes associated with $O_2$ gas diffusion within the porous electrode. Moreover, the capacitance values obtained for this contribution strongly indicate that gas diffusion into the porous electrode is the limiting step [44]. This

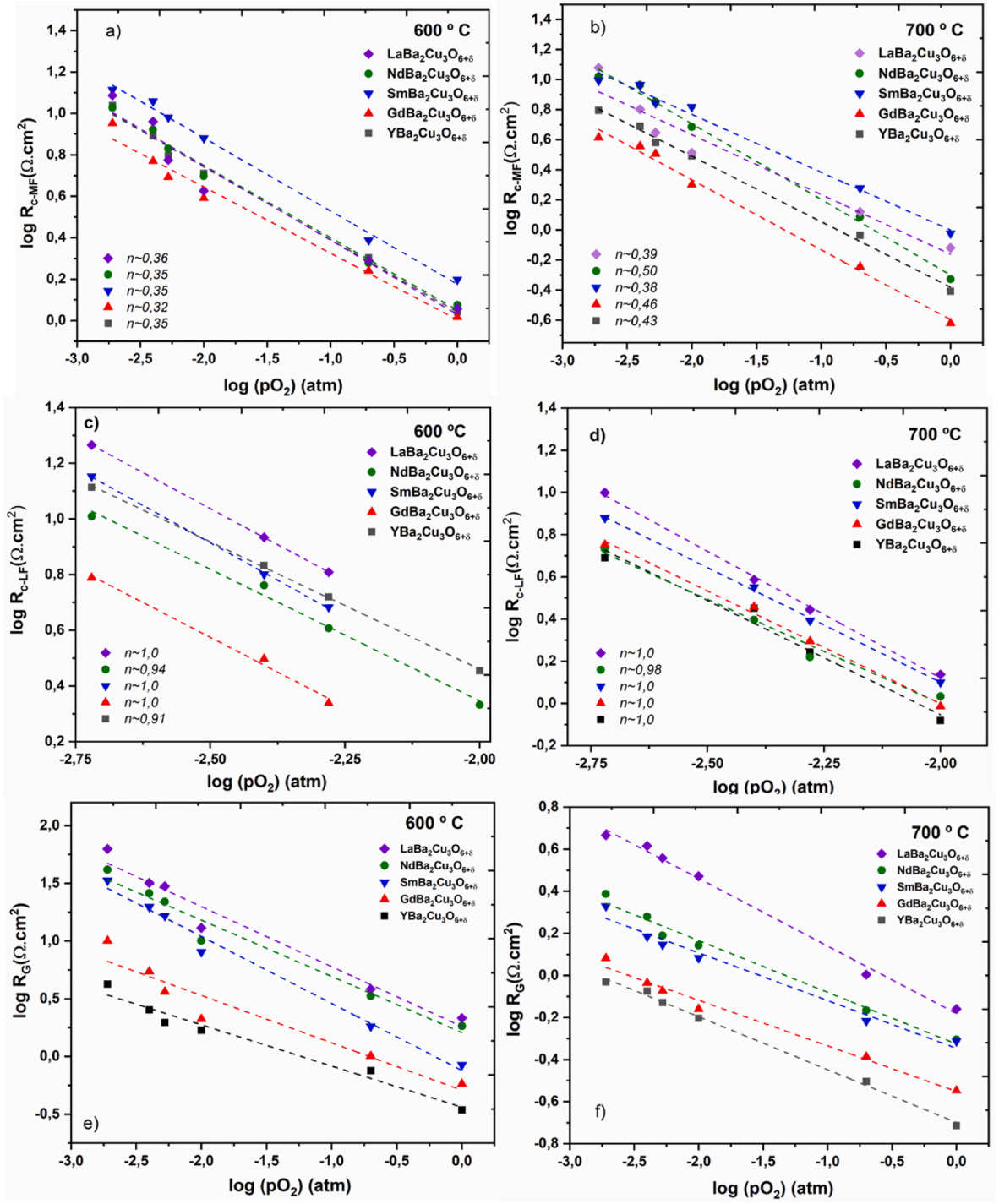


**Fig. 5.** a), b), c) and d) Evolution of the calculated MF and LF polarization resistances at 600 and 700 °C as a function of $pO_2$, respectively, for all REBCO samples; e) and f) evolution of Gerischer resistive component (RG) at 600 and 700 °C.

correlation is consistent with enhanced kinetic energy and increased oxygen molecule mobility at elevated temperatures.

The Gerischer element represent, primarily, the diffusion of species ($O^{2-}$) within the bulk of the Mixed Ionic-Electronic Conductor (MIEC) [45]. The Gerischer impedance is used to model the impedance behaviour of the MIEC, where $O_2$ in the gas phase is reduced at the MIEC|gas| current-collector triple interface in $O^{2-}$, consuming electrons from the collector, then diffuses through the MIEC to the electrolyte phase [46–48]. The chemical reaction involved in the Gerischer impedance is the exchange of oxygen between the gas phase and the MIEC. Fig. 5e and f illustrate the evolution of the resistive component respect to oxygen partial pressure at 600 °C and 700 °C. The calculated values follow the expected evolution predicted by the Adler-Steele-Lane (ASL) model [42, 45,47,48], and the slopes of the fitted curves are consistent with its predictions. The most important feature deduced from the data is the significant decrease in the calculated $R_G$ values with decreasing ionic radius of the $RE^{3+}$ cation. Table 3 summarises the calculated slopes from the linear regression performed.

From the data can be observed that the magnitude of this resistive component is higher than the polarization resistances ($R_{c-MF}$ and $R_{c-LF}$)

**Table 3**
Evolution of the slope of the Gerischer resistive component calculated from ECM for 600 and 700 °C, for all REBCO samples.

| Gerischer Resistive component slope value (*n*) | | | | | |
|---|---|---|---|---|---|
| T (° C) | LBCO | NBCO | SBCO | GBCO | YBCO |
| **600** | 0.52 (4) | 0.49 (4) | 0.58 (3) | 0.41 (6) | 0.35 (3) |
| **700** | 0.32 (1) | 0.24 (1) | 0.22 (1) | 0.21 (2) | 0.20 (1) |

calculated by the model. This fact strongly suggests that ionic diffusion is the rate-limiting step of the reaction once the $O^{2-}$ species forms and incorporates into a vacant site, as follows:

$$O_{2(g)} + 4e^{\cdot} + 2V_O^{\cdot\cdot} \rightarrow 2O_O^x \quad (2)$$

Consequently, the high impedance contribution can be described more accurately as a co-limited process between the oxygen exchange at the electrode/gas surface and the oxygen ion diffusion on the surface and the bulk material [49–51]. Variations in slope value with increasing temperature can be attributed to the transition between semi-infinite and finite-length diffusion models. Sinterization and particle growth phenomena are a consequence of the increasing temperature, in consequence, the effective diffusion length ($l_\delta$) or reaction layer thickness can change, causing the system to shift its behaviour [46].

One of the relevant factors influencing transport in these structures is the free volume ($V_f$), which quantifies the unoccupied space within the unit cell. This is defined as the residual void volume within the cell once the crystallographic sites are occupied by their respective ions. Larger $V_f$ values can be interpreted as indicative of wider migration channels for the diffusion of mobile species ($O^{2-}$ in this context), thereby promoting enhanced transport. Another critical factor directly influencing the migration of oxide ions is the average metal-oxygen (B–O) bond energy. Generally, weaker bonds lead to improved transport in perovskites. It has been reported that the B–O bond energy in perovskite structures is intricately linked to the electronegativity and valence of the metal at the B-site [28].

While these factors are detailed in the literature and widely studied, perovskite-type structures, specifically layered ones, have shown behaviours that are not aligned with the models proposed for cubic structures with 3D transport pathways. Previous reports by Mazo et al. [52] concluded, using Molecular Dynamics (MD) calculations on cuprates, that short distances between similar atomic positions make diffusion in layers advantageous over other possible migration mechanisms. In a recent study, Q. Ji et al. observed that for RP-type structures based on lanthanum-copper oxides doped with barium and strontium [20], the addition of alkaline-earth cations with different ionic radii modifies the Cu–O distance in the structure, thereby altering the energy required for vacancy formation depending on the transition metal cation. This modification has been found to favour incorporation/transport as the Cu–O bond distance increases. The experimental results obtained in this work are consistent with all of these previous reports and other examples [53–56], confirming that in such structures, the Cu–O bond distance is directly related to the electrochemical performance of these materials as electrodes in SOFC/SOEC-type devices, where mass transport occurs through oxide ion or oxygen vacancy diffusion mechanisms.

Furthermore, alterations in the electrochemical behaviour imply that structures of this kind are valuable for exploring potential direct structure-property correlations, as previously indicated by Refs. [17, 57]. Furthermore, it is essential to note that all the prepared cathodes were tested at 800 °C in a complete cell REBCO/YSZ/YSZ-NiO/Ni configuration, showing suitable maximum power density values and comparable with cobalt-free materials and other cuprate cathode performance [9,18,58–61]. A clear correlation emerges between cuprate structures and electrochemical properties when this study is conducted. For REBCO samples, the power density evolution was 152, 180, 253, 330, and 425 $mWcm^{-2}$ for LBCO, NBCO, SBCO, GBCO and YBCO, respectively [23]. Based SEM and XRD data, we have made the assumption that the consistency in crystal structures and microstructures of the materials studied makes the influence of grain surface and defect-related conductivity negligible in this system, allowing us to associate the electrochemical to structural trends. There is no clear indication our assumptions are wrong, but, in the case they were all the conclusions should be re-evaluated under new light.

## 4. Conclusions

This systematic study presents a comprehensive investigation into the oxygen reduction reaction rate-limiting steps (ORR-RLS) in $REBa_2Cu_3O_{6+\delta}$ (RE = La, Nd, Sm, Gd, Y) triple-layered perovskite materials, evaluating their suitability as intermediate-temperature solid oxide fuel cell (IT-SOFC) cathodes. Data suggests that the variation in $RE^{3+}$ ionic indirectly modifies the Cu–O bond distance, a parameter related to ion diffusion. This interdependence establishes the $RE^{3+}$ ionic radius as a key design variable in tailoring cathode performance. The correlation between the ionic radius and vacancy ordering emphasizes crystal structure's pivotal role in determining these perovskite's functional performance.

Electrochemical analysis revealed three distinct contributions to the ORR: a mid-frequency process attributed to charge transfer, which no significant variations with the ionic radius of $RE^{3+}$, a low-frequency process associated with gas-phase diffusion, showing shifts with temperature but independent of structural variations and a bulk/surface diffusion step, where variations in the ionic radii significantly influenced the transport of $O^{2-}$ ions within the structure. The latter was identified as the most influential process due to its resistive component contribution, highlighting the direct connection between the ionic radius, oxygen vacancy and anion mobility within the crystal structure. By elucidating the role of $RE^{3+}$ size, this work provides a pathway for optimizing the design of high-performance IT-SOFC cathodes, advancing the field of energy-efficient and durable SOFC cathode materials.

## CRediT authorship contribution statement

**J. Grassi:** Writing – review & editing, Writing – original draft, Visualization, Validation, Methodology, Investigation, Formal analysis, Data curation, Conceptualization. **A. Montenegro-Hernandez:** Writing – review & editing, Writing – original draft, Visualization, Validation, Methodology, Investigation, Formal analysis, Data curation, Conceptualization. **A.C. Serquis:** Writing – review & editing, Writing – original draft, Visualization, Validation, Methodology, Investigation, Formal analysis, Data curation, Conceptualization. **J.F. Basbus:** Writing – review & editing, Writing – original draft, Visualization, Validation, Methodology, Investigation, Formal analysis, Data curation, Conceptualization. **L. Suescun:** Writing – review & editing, Writing – original draft, Visualization, Validation, Supervision, Resources, Project administration, Methodology, Investigation, Funding acquisition, Formal analysis, Data curation, Conceptualization.

## Declaration of competing interest

The authors declare that they have no known competing financial interests or personal relationships that could have appeared to influence the work reported in this paper.

## Acknowledgements

L.S. and J.G. thank Agencia Nacional de Investigación e Innovación for a PhD Grant POS_NAC_ 2018_1_ 152154 and funding through projects FSE_2015_1_109493 and FMV_2021_ 1_168994 and PEDECIBA – Program for the Development of Basic Sciences (MEC-Udelar) –

Uruguay.

J.G. thanks the **H2ENRY** project, which is subsidized by the Center for Technological Development and Innovation (CDTI) and supported by the Ministry of Science, Innovation and Universities. "*Cervera Excellence Center*".

The authors acknowledge Dr. L. Mogni from DCM-CAB-CNEA for her assistance during EIS experiments and fruitful discussions.

## Appendix A. Supplementary data

Supplementary data to this article can be found online at https://doi.org/10.1016/j.jpcs.2025.113411.

## Data availability

Data will be made available on request.

## References

[1] Y. Lyu, J. Xie, D. Wang, J. Wang, Review of cell performance in solid oxide fuel cells, J. Mater. Sci. 55 (2020) 7184–7207, https://doi.org/10.1007/s10853-020-04497-7.

[2] C. Lenser, D. Udomsilp, N.H. Menzler, P. Holtappels, T. Fujisaki, L. Kwati, H. Matsumoto, A.G. Sabato, F. Smeacetto, A. Chrysanthou, S. Molin, Solid Oxide Fuel and Electrolysis Cells, Elsevier Ltd., 2019, https://doi.org/10.1016/B978-0-08-102726-4.00009-0.

[3] M.I. Dli, A.A. Baliabina, N.V. Drozdova, Hydrogen energy and development prospects, Altern. Energy Ecol. (2016) 37–41, https://doi.org/10.15518/isjaee.2015.22.004.

[4] A.I. Klyndyuk, E.A. Chizhova, D.S. Kharytonau, D.A. Medvedev, Layered oxygen-deficient double perovskites as promising cathode materials for solid oxide fuel cells, Materials (Basel) 15 (2022), https://doi.org/10.3390/ma15010141.

[5] N. Grunbaum, L. Dessemond, J. Fouletier, F. Prado, L. Mogni, A. Caneiro, Rate limiting steps of the porous La0.6Sr0.4Co0.8Fe0.2O3-δ electrode material, Solid State Ionics 180 (2009) 1448–1452, https://doi.org/10.1016/j.ssi.2009.09.005.

[6] T. Wei, Y.H. Huang, R. Zeng, L.X. Yuan, X.L. Hu, W.X. Zhang, L. Jiang, J.Y. Yang, Z. L. Zhang, Evaluation of Ca3 Co2O6 as cathode material for high-performance solid-oxide fuel cell, Sci. Rep. 3 (2013) 1–6, https://doi.org/10.1038/srep01125.

[7] T.A. Zhuravleva, Electrophysical properties of layered perovskites LnBaCo 2-xCuxO 5+δ (Ln = Sm, Nd) for solid oxide fuel cells, Russ. J. Electrochem. 47 (2011) 676–680, https://doi.org/10.1134/S1023193511060164.

[8] V.A. Cherepanov, T.V. Aksenova, L.Y. Gavrilova, K.N. Mikhaleva, Structure, nonstoichiometry and thermal expansion of the NdBa(Co,Fe) 2O5+δ layered perovskite, Solid State Ionics 188 (2011) 53–57, https://doi.org/10.1016/j.ssi.2010.10.021.

[9] K. Li, A. Niemczyk, K. Świerczek, A. Stępień, Y. Naumovich, J. Dąbrowa, M. Zajusz, K. Zheng, B. Dabrowski, Co-free triple perovskite La1.5Ba1.5Cu3O7±δ as a promising air electrode material for solid oxide fuel cells, J. Power Sources 532 (2022), https://doi.org/10.1016/j.jpowsour.2022.231371.

[10] W. Zhou, R. Ran, Z. Shao, W. Zhuang, J. Jia, H. Gu, W. Jin, N. Xu, Barium- and strontium-enriched (Ba0.5Sr0.5)1+xCo0.8Fe0.2O3-δ oxides as high-performance cathodes for intermediate-temperature solid-oxide fuel cells, Acta Mater. 56 (2008) 2687–2698, https://doi.org/10.1016/j.actamat.2008.02.002.

[11] A. Esquirol, N.P. Brandon, J.A. Kilner, M. Mogensen, Electrochemical characterization of La[sub 0.6]Sr[sub 0.4]Co[sub 0.2]Fe[sub 0.8]O[sub 3] cathodes for intermediate-temperature SOFCs, J. Electrochem. Soc. 151 (2004) A1847, https://doi.org/10.1149/1.1799391.

[12] K. Yakal-Kremski, L.V. Mogni, A. Montenegro-Hernández, A. Caneiro, S.A. Barnett, Determination of electrode oxygen transport kinetics using electrochemical impedance spectroscopy combined with three-dimensional microstructure measurement: application to Nd 2 NiO 4+δ, J. Electrochem. Soc. 161 (2014) F1366–F1374, https://doi.org/10.1149/2.0521414jes.

[13] A. Niemczyk, K. Zheng, K. Cichy, K. Berent, K. Küster, U. Starke, B. Poudel, B. Dabrowski, K. Świerczek, High Cu content LaNi1-xCuxO3-δ perovskites as candidate air electrode materials for reversible solid oxide cells, Int. J. Hydrogen Energy 45 (2020) 29449–29464, https://doi.org/10.1016/j.ijhydene.2020.07.267.

[14] A. Niemczyk, Z. Du, A. Olszewska, M. Marzec, M. Gajewska, K. Świerczek, H. Zhao, B. Poudel, B. Dabrowski, Effective oxygen reduction on A-site substituted LaCuO3-: δ: toward air electrodes for SOFCs based on perovskite-type copper oxides, J. Mater. Chem. A 7 (2019) 27403–27416, https://doi.org/10.1039/c9ta09244g.

[15] V.V. Kharton, F.M.B. Marques, A. Atkinson, Transport properties of solid oxide electrolyte ceramics: a brief review, Solid State Ionics 174 (2004) 135–149, https://doi.org/10.1016/j.ssi.2004.06.015.

[16] J.F. Basbus, F.D. Prado, A. Caneiro, L.V. Mogni, A comparative study of high temperature properties of cobalt-free perovskites, J. Electroceram. 32 (2014) 311–318, https://doi.org/10.1007/s10832-014-9901-9.

[17] G.N. Mazo, S.M. Kazakov, L.M. Kolchina, S.Y. Istomin, E.V. Antipov, N.V. Lyskov, M.Z. Galin, L.S. Leonova, Y.S. Fedotov, S.I. Bredikhin, Y. Liu, G. Svensson, Z. Shen, Influence of structural arrangement of R2O2 slabs of layered cuprates on high-temperature properties important for application in IT-SOFC, Solid State Ionics 257 (2014) 67–74, https://doi.org/10.1016/j.ssi.2014.01.039.

[18] X. Hu, M. Li, Y. Xie, Y. Yang, X. Wu, C. Xia, Oxygen-deficient ruddlesden-popper-type lanthanum strontium cuprate doped with bismuth as a cathode for solid oxide fuel cells, ACS Appl. Mater. Interfaces (2019), https://doi.org/10.1021/acsami.9b05445.

[19] X. Meng, S. Lü, W.W. Yu, Y. Ji, Y. Sui, M. Wei, Layered perovskite LnBa0.5Sr0.5Cu2O5+Δ (Ln = Pr and Nd) as cobalt-free cathode materials for solid oxide fuel cells, Int. J. Hydrogen Energy 43 (2018) 4458–4470, https://doi.org/10.1016/j.ijhydene.2018.01.033.

[20] Q. Ji, J. Meng, H. Wang, T. An, J. Meng, X. Liu, Ruddlesden-Popper-based lanthanum cuprate thin film cathodes for solid oxide fuel cells: effects of doping and structural transformation on the oxygen reduction reaction, Int. J. Hydrogen Energy 46 (2021) 27173–27182, https://doi.org/10.1016/j.ijhydene.2021.05.170.

[21] A. Harabor, P. Rotaru, N.A. Harabor, P. Nozar, A. Rotaru, Orthorhombic YBCO-123 ceramic oxide superconductor: structural, resistive and thermal properties, Ceram. Int. 45 (2019) 2899–2907, https://doi.org/10.1016/j.ceramint.2018.07.272.

[22] J. Grassi, M.A. Macías, J.F. Basbus, J. Castiglioni, G.H. Gauthier, A.C. Serquis, L. Suescun, Synthesis and characterization of high temperature properties of YBa2Cu3O6+δ superconductor as potential cathode for intermediate temperature solid oxide fuel cells, J. Mater. Sci. Technol. Res. 8 (2021) 82–91, https://doi.org/10.31875/2410-4701.2021.08.10.

[23] J. Grassi, N. Di Benedetto, M.A. Macías, J. Basbus, A. Serquis, L. Suescun, Power density vs ionic radii correlations in REBa2Cu3O6+δ (RE = La, Nd, Sm, Gd and Y) IT – SOFC potential cathodes, Electrochim. Acta 464 (2023) 142931, https://doi.org/10.1016/j.electacta.2023.142931.

[24] G. Cordaro, A. Flura, A. Donazzi, R. Pelosato, F. Mauvy, C. Cristiani, G. Dotelli, J.-C. Grenier, Synthesis and characterization of praseodymium cuprates compounds as innovative and efficient oxygen electrode for IT-SOFCs, ECS Trans. 91 (2019) 1279–1289, https://doi.org/10.1149/09101.1279ecst.

[25] R. von D. Larson, A, General Structure Analysis System (GSAS), LAUR, 2004, pp. 86–748.

[26] C.A. Schneider, W.S. Rasband, K.W. Eliceiri, NIH image to ImageJ: 25 years of image analysis, Nat. Methods 9 (2012) 671–675, https://doi.org/10.1038/nmeth.2089.

[27] A. Caneiro, M. Bonnat, J. Fouletier, Measurement and regulation of oxygen content in selected gases using solid electrolyte cells. IV. Accurate preparation of CO2-CO and H2O-H2 mixtures, J. Appl. Electrochem. 11 (1981) 83–90, https://doi.org/10.1007/BF00615326.

[28] W. Li, J. Sunarso, Y. Yang, Y. Chen, C. Ge, W. Wang, Y. Guo, R. Ran, W. Zhou, Strategies for improving oxygen ionic conducting in perovskite oxides and their practical applications, Energy Rev. 3 (2024) 100085, https://doi.org/10.1016/j.enrev.2024.100085.

[29] A. Petri, P. Huang, Oxygen condcutivity of Nd(Sr/Ca) Ga(Mg)O3-d perovskites, Solid State Ionics 92 (1996) 113–117.

[30] T. Ishihara, H. Furutani, H. Arikawa, M. Honda, T. Akbay, Y. Takita, Oxide ion conductivity in doubly doped PrGaO3 perovskite-type oxide, J. Electrochem. Soc. 146 (1999) 1643–1649, https://doi.org/10.1149/1.1391820.

[31] Y. Takeda, R. Kanno, M. Noda, Y. Tomida, O. Yamamoto, Cathodic polarization phenomena of perovskite oxide electrodes with stabilized zirconia, J. Electrochem. Soc. 134 (1987) 2656–2661, https://doi.org/10.1149/1.2100267.

[32] M.J. Escudero, A. Aguadero, J.A. Alonso, L. Daza, A kinetic study of oxygen reduction reaction on La2NiO4 cathodes by means of impedance spectroscopy, J. Electroanal. Chem. 611 (2007) 107–116, https://doi.org/10.1016/j.jelechem.2007.08.006.

[33] Y. Gu, Y. Zhang, Y. Zheng, H. Chen, L. Ge, L. Guo, PrBaMn2O5+Δ with praseodymium oxide nano-catalyst as electrode for symmetrical solid oxide fuel cells, Appl. Catal. B Environ. 257 (2019) 117868, https://doi.org/10.1016/j.apcatb.2019.117868.

[34] A.P. Khandale, S.S. Bhoga, An investigation of different Nd1.8Ce0.2CuO 4+δ-Ce0.9Gd0.1O2-δ composite cathodes, Electrochim. Acta 130 (2014) 439–445, https://doi.org/10.1016/j.electacta.2014.03.031.

[35] Q. Ni, H. Chen, L. Ge, S. Yu, L. Guo, Investigation of La1−xSmx−ySryCoO3−Δcathode for intermediate temperature solid oxide fuel cells, J. Power Sources 349 (2017) 130–137, https://doi.org/10.1016/j.jpowsour.2017.03.037.

[36] Z. Du, C. Yan, H. Zhao, Y. Zhang, C. Yang, S. Yi, Y. Lu, K. Świerczek, Effective Ca-doping in Y1-: XCaxBaCo2O5+ δ cathode materials for intermediate temperature solid oxide fuel cells, J. Mater. Chem. A 5 (2017) 25641–25651, https://doi.org/10.1039/c7ta08954f.

[37] S. Mulmi, V. Thangadurai, A perovskite-type Nd0.75Sr0.25Co0.8Fe0.2O3-: δ cathode for advanced solid oxide fuel cells, Chem. Commun. 55 (2019) 3713–3716, https://doi.org/10.1039/c9cc01054h.

[38] Z. Jiang, Z. Lei, B. Ding, C. Xia, F. Zhao, F. Chen, Electrochemical characteristics of solid oxide fuel cell cathodes prepared by infiltrating (La,Sr)MnO3 nanoparticles into yttria-stabilized bismuth oxide backbones, Int. J. Hydrogen Energy 35 (2010) 8322–8330, https://doi.org/10.1016/j.ijhydene.2009.12.008.

[39] S.B. Adler, Factors governing oxygen reduction in solid oxide fuel cell cathodes, Chem. Rev. 104 (2004) 4791–4844, https://doi.org/10.1021/cr020724o.

[40] C. Diandian, H. Bala, Z. Bowen, Z. Zhiyong, Improving the Stability and Efficiency of Perovskite Solar Cells by Controlling the Crystallization Active Layer with Binary Anti-solvent, vol. 40, 2024, pp. 1160–1170.

[41] Y. Li, R. Gemmen, X. Liu, Oxygen reduction and transportation mechanisms in solid oxide fuel cell cathodes, J. Power Sources 195 (2010) 3345–3358, https://doi.org/10.1016/j.jpowsour.2009.12.062.

[42] S.H. Chan, X.J. Chen, K.A. Khor, Cathode micromodel of solid oxide fuel cell, J. Electrochem. Soc. 151 (2004) A164, https://doi.org/10.1149/1.1630036.
[43] A.C. Co, S.J. Xia, V.I. Birss, A kinetic study of the oxygen reduction reaction at LaSrMnO[sub 3]-YSZ composite electrodes, J. Electrochem. Soc. 152 (2005) A570, https://doi.org/10.1149/1.1859612.
[44] S.P. Yoon, S.W. Nam, J. Han, T.H. Lim, S.A. Hong, S.H. Hyun, Effect of electrode microstructure on gas-phase diffusion in solid oxide fuel cells, Solid State Ionics 166 (2004) 1–11, https://doi.org/10.1016/j.ssi.2003.10.010.
[45] B.A. Boukamp, H.J.M. Bouwmeester, Interpretation of the gerischer impedance in solid state ionics, Solid State Ionics 157 (2003) 29–33, https://doi.org/10.1016/S0167-2738(02)00185-6.
[46] S.B. Adler, J.A. Lane, B.C.H. Steele, Electrode kinetics of porous mixed-conducting oxygen electrodes, J. Electrochem. Soc. 143 (1996) 3554–3564, https://doi.org/10.1149/1.1837252.
[47] A. Flura, C. Nicollet, V. Vibhu, B. Zeimetz, A. Rougier, J.-M. Bassat, J.-C. Grenier, Application of the Adler-Lane-Steele Model to Porous La 2 NiO 4+ δ SOFC Cathode: influence of Interfaces with Gadolinia Doped Ceria, J. Electrochem. Soc. 163 (2016) F523–F532, https://doi.org/10.1149/2.0891606jes.
[48] L. Yasin, A. Atkinson, S.J. Cooper, A. Bertei, Identifiability of the mechanisms governing the reaction kinetics of MIEC electrodes in solid oxide cells, Electrochim. Acta 472 (2023) 143418, https://doi.org/10.1016/j.electacta.2023.143418.
[49] J. Nielsen, J. Hjelm, Impedance of SOFC electrodes: a review and a comprehensive case study on the impedance of LSM:YSZ cathodes, Electrochim. Acta 115 (2014) 31–45, https://doi.org/10.1016/j.electacta.2013.10.053.
[50] L.V. Mogni, Estudio De Nuevos Conductores Mixtos Para Aplicaciones Electroquímicas De Alta Temperatura, 2007.
[51] A., M. Interpretation of the Performance and Degradation of Reformate Fueled Solid Oxide Fuel Cells, vol. 24, K.S.P. Kromp, No Title, 2014 n.d.
[52] G.N. Mazo, S.N. Savvin, V. V Petrykin, I.A. Koudriashov, Oxygen Mobility in Layered Cuprates La Sr CuO 2yx X 4yd, n.d. www.elsevier.comrlocaterssi..
[53] K. Zheng, A. Gorzkowska-Sobaś, K. Świerczek, Evaluation of Ln 2CuO 4 (Ln: la, Pr, Nd) oxides as cathode materials for IT-SOFCs, Mater. Res. Bull. 47 (2012) 4089–4095, https://doi.org/10.1016/j.materresbull.2012.08.072.
[54] S.J. Lee, P. Muralidharan, S.H. Jo, D.K. Kim, Composite cathode for IT-SOFC: Sr-doped lanthanum cuprate and Gd-doped ceria, Electrochem. Commun. 12 (2010) 808–811, https://doi.org/10.1016/j.elecom.2010.03.039.
[55] N.V. Lyskov, L.M. Kolchina, M.Z. Galin, G.N. Mazo, Development of lanthanum-doped praseodymium cuprates as cathode materials for intermediate-temperature solid oxide fuel cells, Solid State Ionics 319 (2018) 156–161, https://doi.org/10.1016/j.ssi.2018.02.017.
[56] M.S. Kaluzhskikh, S.M. Kazakov, G.N. Mazo, S.Y. Istomin, E.V. Antipov, A. A. Gippius, Y. Fedotov, S.I. Bredikhin, Y. Liu, G. Svensson, Z. Shen, High-temperature crystal structure and transport properties of the layered cuprates Ln2CuO4, Ln=Pr, Nd and Sm, J. Solid State Chem. 184 (2011) 698–704, https://doi.org/10.1016/j.jssc.2011.01.035.
[57] N.V. Lyskov, L.M. Kolchina, P.P. Pestrikov, G.N. Mazo, E.V. Antipov, Electrotransport properties of SOFC cathode materials based on lanthanum cuprate doped with praseodymium and strontium oxides, Russ. J. Electrochem. 52 (2016) 642–647, https://doi.org/10.1134/S1023193516070120.